Multispectral measurement of scattering-angular light distribution in apple skin and flesh samples

Mohamed Lamine Askoura, Fabrice Vaudelle, Jean-Pierre L'huillier

Mohamed Lamine Askoura, Fabrice Vaudelle, Jean-Pierre L'huillier. Multispectral measurement of scattering-angular light distribution in apple skin and flesh samples. Applied Optics, 2016, 55 (32), pp.9217. hal-02333709

Multispectral measurement of scattering-angular light distribution in apple skin and flesh samples

MOHAMED LAMINE ASKOURA, FABRICE VAUDELLE,* AND JEAN-PIERRE L'HUILLIER

Université Bretagne Loire, Ecole Nationale Supérieure des Arts-et-Métiers (ENSAM), LAMPA, 2 Bd du Ronceray, BP 93525, 49035 Angers Cedex 01, France
**Corresponding author: f.vaudelle@libertysurf.fr*

Knowledge of the optical properties of apple tissues such as skin and flesh is essential to better understand the light–tissue interaction process and to apply optical methods for apple quality inspection. This work aimed at estimating the anisotropy factor of thin skin and flesh samples extracted from three apple cultivars. The scatter-ing-angular light distribution in each tissue sample was measured at four wavelengths ($\lambda = 633, 763, 784$, and 852 nm), by means of a goniometer setup. Based on the recorded angular intensity $I(\theta,\lambda)$, the effective anisotropy factor g_{eff} of each tissue type was first estimated using the mean statistics applied to the random variable $\cos\theta$. Next, the measured data were fitted with three predefined and modified phase functions—Henyey-Greenstein (p_{MHG}), Gegenbauer kernel (p_{MGK}), and Mie (p_{Mie})—in order to retrieve the corresponding anisotropy factors g_{MHG}, g_{MGK}, and $g_{M\,\mathrm{Mie}}$. Typically, the anisotropy factors of skin and flesh amount to 0.6–0.8 in the above-mentioned wavelength range.

http://dx.doi.org/10.1364/AO.55.009217

1. INTRODUCTION

Light emitted at wavelengths ranging from visible to near-infrared is commonly used to noninvasively diagnose biological tissues [1–3] or to assess internal quality attributes of various fruits and vegetables [4]. Near-infrared radiation can reasonably penetrate into tissues, then offering a potential spectral window without effects of ionizing radiations. The attenuation of light into the interrogated tissue is mainly due to absorption and scattering processes, while reflected and/or transmitted light re-emerging from the boundaries follows very complicated paths. These complex events may be characterized by four key optical parameters such as the absorption and scattering coefficients, the scattering phase function, and the average refractive index n. The absorption coefficient μ_a and the scattering coefficient μ_s are, respectively, the number of absorption and scattering events per unit length, while the scattering phase function $p(\theta)$ represents the probability of a photon being scattered in a certain direction. In the case of a strongly scattering regime (high number of scattering events), the inverse of the average distance between consecutive scattering events is defined as the reduced scattering coefficient μ_s' so that $\mu_s' = \mu_s(1 - g)$, where g (anisotropy factor) is the average cosine of the angular deviation.

For quality inspection of apples, it is essential to retrieve and uncouple (as much as possible) μ_a and μ_s'. Time-resolved reflectance spectroscopy [5–7] and multispectral/hyperspectral spatially resolved imaging [8–11] have been extensively used to extract the apple flesh optical properties. These optical methods are rather sensitive to the flatness of the sensing boundary, because absorption and scattering information is acquired from an inverse algorithm generally based on a semi-infinite (homogeneous) diffusion model [12,13].

Another important point is that the light must travel through a thin skin layer before reaching the apple flesh and re-emerging from the tissue–air boundary. Because the skin has different optical properties with respect to those of the flesh [14], reflectance measurements may be influenced, especially for short source–detector distances [15]. A correct interpretation of measured reflectance signals requires the use of the radiative transfer equation (RTE) [2,3] to model light propagation in the fruit, still considering μ_a, μ_s, and $p(\theta)$ of each tissue type. A usual way to numerically solve the RTE is to use the Monte Carlo method [16], which simulates photon paths according to probability density functions for the step size between photon–tissue interaction sites and the angles of deflection. Theoretically, Monte Carlo solutions can be obtained for any desired accuracy without limitations of complex geometries [17–21] and optical properties. The phase function $p(\theta)$ and its first moment g can be experimentally determined by irradiating thin samples of the considered media with a laser beam, and performing angular scattering measurements in a goniometer setup. Although the method requires that multiple scattering in the sample be negligible, i.e., thickness $<1/\mu_s$, the angular distributions of different tissues and biomaterials have been successfully reported [22–29]. More recently, the method was improved to predict $p(\theta)$ and g for thick tissue samples [30].

To our knowledge, few works deal with the scattering anisotropy factors of apple skin and flesh, except for hyperspectral data reported in [14], and obtained by using an integrating sphere technique combined with the inverse adding-doubling method.

In this paper, the anisotropy factors of thin skin and flesh samples extracted from three apple cultivars are experimentally determined thanks to a goniometer setup. For each tissue sample, the angular intensities of scattered light were then measured under repeatability conditions at four wavelengths of 633, 763, 784, and 852 nm. In the same conditions, the shape of three modified scattering phase functions was fitted with the experimental data. A primary objective was to ascertain a range of g and $p(\theta)$ values that typify soft apple tissues at these wavelengths. These optical properties are important to improve the features of a Monte Carlo model, which allows us to simulate light transport in an apple modeled as a two-layer spherical tissue structure [19,20].

The paper is set out as follows: Section 2 presents the experimental apparatus, the tissue sample characteristics, and experimental methods. Analysis of angular scattering measurements and fitting results based on the three predefined scattering phase functions appears in Section 3. Section 4 discusses the accumulated experimental data and their implications.

2. MATERIALS AND METHODS

A. Goniometric Setup and Tissue Samples

The apparatus used to measure the angular intensities of scattered light by skin and flesh samples is illustrated in Figs. 1(a) and 1(b). The sample was placed at the center of the equatorial plane of a 30 cm diameter spherical glass tank filled with distilled water, and irradiated by the laser beam selected among four light sources emitting at 633, 763, 784, and 852 nm. The average beam power of each laser was maintained at 20 mW. The water was filtered to minimize light scattering due to residual dust particles. Its role is to prevent the refraction of scattered photons and to maintain the sample hydrated during the experiments. Furthermore, a light baffle was placed between the laser source and the glass tank to attenuate the background light. The scattered light is captured at the angular position θ by a photodiode system, which was fixed on a detector arm. This arm was manually rotated around the tank so that the active part of the detector (optical fiber and slit assembly) remained in the plane of the laser beam (i.e., the equatorial plane). The scattered light measurements were made in the range of 0°–165°, with an error in positioning of the detector arm equal to ±0.2°. The sample (skin or flesh) thicknesses were chosen as small as possible in order to minimize multiple scattering events ($\leq 75-100\ \mu\text{m}$ for the skin, $\leq 330\ \mu\text{m}$ for the flesh as adapted from data reported in [14]). Skin samples were removed from three apple cultivars (Royal Gala, Golden Delicious, and Granny Smith), whereas flesh samples were sliced in the heart of these same fruits. The apple cultivars were kept at room temperature (20°C) for at least 2 h before the tissue samples (skin/flesh) were extracted. They were randomly selected from the storage without considering the harvest. Only two flesh and skin samples were extracted from each apple cultivar. These samples were chosen as the most representative of the batch (without defects). The remaining flesh covering one side of the extracted skin was scraped off using a razor blade, so only the apple skin sample remained. Typically, the mean measured thicknesses of the skin (flesh) samples were 183 μm (400 μm), 127 μm (290 μm), and 100 μm (280 μm) for Gala, Golden, and Granny, respectively. Each sample was fixed on an open rectangular holder as depicted in Fig. 1(b).

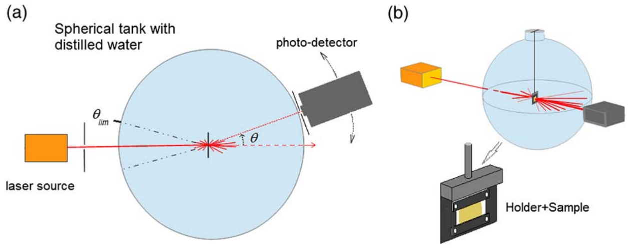

Fig. 1. Experimental setup. (a) Description in a scattering plane. (b) Sample is put at the center of a spherical glass tank.

B. Scattering Phase Functions

Three predefined phase functions were used to fit the experimental data: the modified Henyey-Greenstein phase function $p_{\text{MHG}}(\theta)$, the modified Gegenbauer kernel phase function $p_{\text{MGK}}(\theta)$, and the modified scattering Mie phase function $p_{M\text{Mie}}(\theta)$.

1. Modified Henyey-Greenstein Phase Function

The Henyey-Greenstein phase function [31] has been widely adapted in the biomedical field to model light propagation in tissue [23]. The p_{HG} phase function is given by Eq. (1):

$$p_{\text{HG}}(\theta) = \frac{1}{4\pi} \frac{1 - g_{\text{HG}}^2}{(1 + g_{\text{HG}}^2 - 2g_{\text{HG}} \cos\theta)^{3/2}}. \tag{1}$$

The modified Henyey-Greenstein phase function, $p_{\text{MHG}}(\theta)$, results from the composition of the single $p_{\text{HG}}(\theta)$ with an additional phase function $p(\theta)$ weighted by a factor f [23,32,33], such that

$$p_{\text{MHG}}(\theta) = (1 - f) \cdot p_{\text{HG}}(\theta) + f p(\theta). \tag{2}$$

The modified anisotropy factor is then calculated as

$$g_{\text{MHG}} = (1 - f) g_{\text{HG}}. \tag{3}$$

2. Modified Gegenbauer Kernel Phase Function

A second commonly used phase function is the Gegenbauer kernel phase function [34]

$$p_{\text{GK}}(\theta) = \frac{\alpha g_\alpha}{\pi[(1 + g_\alpha)^{2\alpha} - (1 - g_\alpha)^{2\alpha}]} \frac{(1 - g_\alpha^2)^{2\alpha}}{(1 + g_\alpha^2 - 2g_\alpha \cos\theta)^{\alpha+1}}. \tag{4}$$

The modified Gegenbauer kernel phase function is then written as

$$p_{\mathrm{MGK}}(\theta) = (1-f)p_{\mathrm{GK}}(\theta) + f p(\theta). \tag{5}$$

The anisotropy factors related to $p_{\mathrm{GK}}(\theta)$ and $p_{\mathrm{MGK}}(\theta)$ are

$$g_{\mathrm{GK}} = \frac{2g_\alpha \alpha \frac{(1+g_\alpha)^{2\alpha}+(1-g_\alpha)^{2\alpha}}{(1+g_\alpha)^{2\alpha}-(1-g_\alpha)^{2\alpha}} - (1+g_\alpha^2)}{2g_\alpha(\alpha-1)} \tag{6}$$

and

$$g_{\mathrm{MGK}} = (1-f)g_{\mathrm{GK}}. \tag{7}$$

This function has three free parameters α, g_α, and f, which should be recovered using a Levenberg–Marquardt algorithm.

3. Modified Scattering Mie Phase Function

Finally, a third modified phase function, $p_{M\mathrm{Mie}}(\theta)$, was used:

$$p_{M\mathrm{Mie}}(\theta) = (1-f)p_{\mathrm{Mie}}(\theta) + f p(\theta), \tag{8}$$

$$p_{\mathrm{Mie}}(\theta) = \frac{\sum_{i=1}^{N} \mu_{s,i} P_{\mathrm{Mie}}(x_i, \theta)}{\sum_{i=1}^{N} \mu_{s,i} \int P_{\mathrm{Mie}}(x_i, \theta) \mathrm{d}\cos\theta}, \tag{9}$$

where P_{Mie} is the scattering intensity [35] (see Appendix B), x_i is the size parameter, and $\mu_{s,i}$ is the scattering coefficient related to a type of particle i having a radius r_i and illuminated by a light of wavelength λ. The scattering coefficient μ_{si} is related to a radius r_i^k, where each k (≤ 40) corresponds to a radius distributed in the interval $[r_i - 0.15r_i < r_i^k < r_i + 0.15r_i]$ following a normal law. Six typical values of radius r_i were chosen (0.15, 0.3, 0.6, 0.9, 1.2, and 1.5 µm). A single scattering coefficient was estimated using $\mu_{s,i}^k = \rho_i \pi (r_i^k)^2 Q_{\mathrm{scat},i}^k$ (Q_{scat} being the Mie scattering efficiency [35]), considering that ρ_i is constant on the interval $[r_i - 0.15r_i,\ r_i + 0.15r_i]$. One ρ_i represents the density of particles for which the radius belongs to one of the six above-defined intervals. The seven parameters ($6\rho_i$, f) should be determined using a Levenberg–Marquardt algorithm. The anisotropy related to $p_{M\mathrm{Mie}}(\theta)$ is

$$g_{M\mathrm{Mie}} = (1-f)g_{\mathrm{Mie}}, \tag{10}$$

with

$$g_{\mathrm{Mie}} = \frac{\sum_{i=1}^{N} \mu_{s,i} \int P_{\mathrm{Mie}}(x_i, \theta) \cos\theta \mathrm{d}\cos\theta}{\sum_{i=1}^{N} \mu_{s,i} \int P_{\mathrm{Mie}}(x_i, \theta) \mathrm{d}\cos\theta}. \tag{11}$$

3. RESULTS

A. Effective Anisotropy Factor g_{eff}

Figures 2(a) and 2(b) show the experimental values for $I(\theta)$ versus θ obtained for the flesh and skin samples irradiated at four wavelengths (633, 763, 784, and 852 nm). Each tissue sample is representative of the apple variety "Golden Delicious." It can be well observed that the collimated light intensity transmitted around the axis ($\theta \sim 0°$) by the flesh sample is notably stronger (4–5 times) than the one transmitted by the skin sample. Moreover, the light intensity recorded in the range of small angles ($1° \leq \theta \leq 6°$) decreases more rapidly in the case of the flesh sample compared with the case of the skin sample. These facts suggest that the microstructure of the flesh [36] allows the light to propagate in a preferential direction with a notable forward on-axis light component (($\theta \sim 0°$), and that the full scattering regime may not be well established until the detecting angle $\theta \sim 6°$ is reached. It is also interesting to note that all the curves reach a minimum around $\theta = 90°$. However, $I(\theta)$ was not well determined for scattering angles between 80° and 100° essentially due to the edges of the sample holder. Furthermore, the raw data show the highly forward nature of the scattering in tissue (skin or flesh), with a backward component not negligible from 100° to 165°.

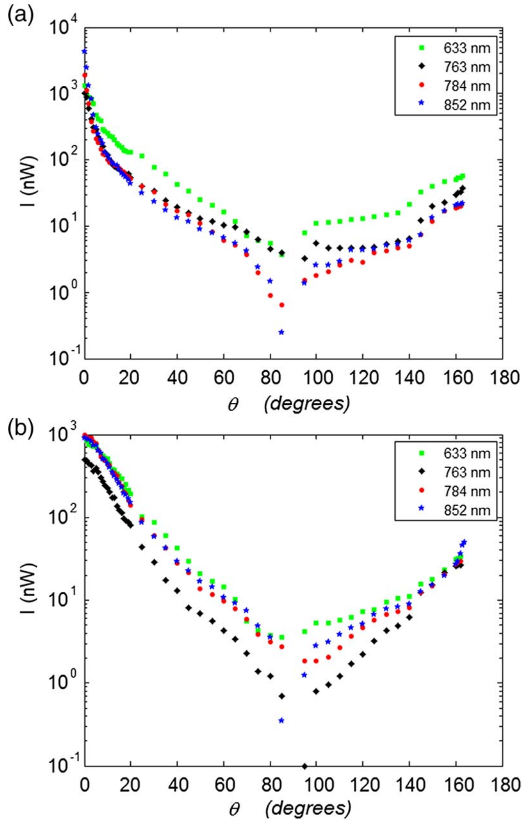

Fig. 2. Experimental values $I(\theta)$ versus θ obtained for (a) flesh and (b) skin samples irradiated at four wavelengths (633, 763, 784, and 852 nm).

The plots for flesh and skin samples related to the two other apple varieties (Royal Gala and Granny Smith) are not presented since they show the same trends as those observed in Figs. 2(a) and 2(b). For all studied tissues, each experiment was repeated three times and the mean values of measured data were used to depict $I(\theta)$ versus θ.

To obtain g_{eff} (defined for the angle space $0° \leq \theta \leq 165°$) of each tissue sample, we considered the basic relationship for the anisotropy g,

$$g = \frac{\int_0^{2\pi} I(\theta) \cos\theta \,\mathrm{d}(\cos\theta)}{\int_0^{2\pi} I(\theta) \mathrm{d}(\cos\theta)} = \frac{\int_0^{2\pi} I(\theta) \cos\theta \ \sin\theta \,\mathrm{d}\theta}{\int_0^{2\pi} I(\theta) \sin\theta \,\mathrm{d}\theta} \tag{12}$$

and then used a discrete version [Eq. (13)] with different angle steps: 1° for $0 \leq \theta \leq 20°$, 5° for $20° < \theta < 160°$, and 1° for $160° \leq \theta \leq 165°$:

$$g_{\mathrm{eff}} = \frac{\sum_k^{N\max} I(\theta_k) \cos\theta_k \ \sin\theta_k \Delta\theta_k}{\sum_k^{N\max} I(\theta_k) \sin\theta_k \Delta\theta_k}. \tag{13}$$

Table 1. Effective Anisotropy in the Forward and Backward Directions g_{eff} and Effective Anisotropy in the Forward Direction g_{forw} for Skin and Flesh Samples

Gala Flesh			**Golden Flesh**			**Granny Flesh**		
λ (nm)	**g_{eff}**	**g_{forw}**	**λ (nm)**	**g_{eff}**	**g_{forw}**	**λ (nm)**	**g_{eff}**	**g_{forw}**
633	0.562	0.691	633	0.410	0.590	633	0.365	0.554
763	0.606	0.717	763	0.418	0.582	763	0.539	0.664
784	0.647	0.736	784	0.537	0.671	784	0.539	0.669
852	0.714	0.772	852	0.516	0.664	852	0.482	0.637
Gala Skin			**Golden Skin**			**Granny Skin**		
λ (nm)	g_{eff}	g_{forw}	λ (nm)	g_{eff}	g_{forw}	λ (nm)	g_{eff}	g_{forw}
633	0.547	0.681	633	0.653	0.742	633	0.651	0.739
763	0.599	0.719	763	0.596	0.731	763	0.685	0.766
784	0.684	0.772	784	0.688	0.771	784	0.739	0.793
852	0.601	0.717	852	0.651	0.749	852	0.747	0.803

The calculated values of g_{eff} in the forward and backward directions and g_{forw} defined for $0° < \theta < 90°$ are listed in Table 1, for skin and flesh samples. The calculations confirm that the scattering is forward peaked for both tissue types ($g_{\mathrm{forw}} \sim 0.75$/skin ~ 0.65/flesh). However, substantially lower values were found for g_{eff}, due to negative values measured in the backward direction (~100°–165°).

B. Use of Predefined Scattering Phase Functions

The use of the three modified scattering phase functions requires us to define the second term $p(\theta)$ in Eqs. (2), (5), and (8). Jacques *et al.* [23] showed that $p(\theta) = 1/4\pi$ for $120° \leq \theta \leq 155°$ in the case of isotropic scattering with limited magnitude. This implies that the observed radiant intensities are divided by $\cos\theta$ in order to correct for Lambert's law. Bevilacqua and Depeursinge [33] proposed $p(\theta) = (3/4\pi)\cos^2\theta$ as an adding term to the Henyey-Greenstein phase function, to better describe the light propagation in turbid media at short source–detector separations. The effects of these two proposed terms $p(\theta)$ have been systematically examined on measurements carried out for large scattering angles ($120° \leq \theta \leq 155°$). Typical results are displayed in Figs. 3(a) and 3(b). It is clearly shown that when the measurements $I(\theta)$ are divided by a function close to $\cos^2\theta$, the results are approximately reduced to a constant b. Note that the added phase delay of 5° has the effect to slightly reduce the value of b, but also to strongly attenuate a residual term at around $\theta = 120°$–$130°$ [see Fig. 3(b)]. In contrast, the measurements treated in the same fashion with $\cos\theta$ do not give useful results. These findings suggest that the angular measurements are governed by a Rayleigh scattering process rather than by Lambert's law. A possible explanation may be due to the presence of scattering particles embedded in both skin and flesh samples, whose size parameters are small compared with the working wavelength [21].

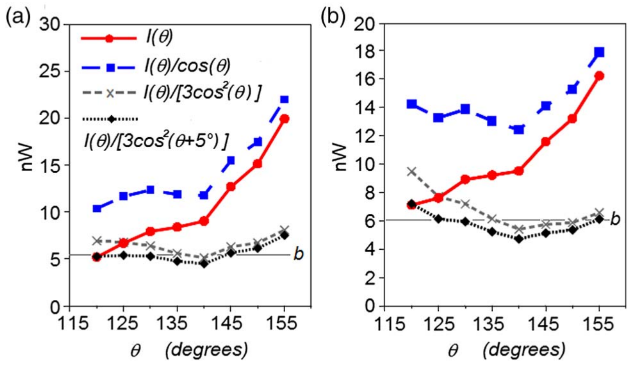

Fig. 3. Validity of $p(\theta) \sim \cos^2\theta$ for measurements ranging from 120° to 155°. (a) Skin sample (Golden Delicious) studied at 852 nm. (b) Flesh sample (Royal Gala) studied at 763 nm.

In order to fit the experiments with the modified Henyey-Greenstein function, $p_{\mathrm{MHG}}(\theta)$, it is interesting to use the transformation proposed in Ref. [23] to find the anisotropy coefficients g_{HG} and g_{MHG}. Let us first substitute Eq. (2) in the transformed Eq. (1). We get

$$[p_{\mathrm{MHG}}(\theta) - f p(\theta)]^{-\frac{2}{3}} = [1 + g_{\mathrm{HG}}^2 - 2g_{\mathrm{HG}}\cos\theta]\left[\frac{(1-f)(1-g_{\mathrm{HG}}^2)}{4\pi}\right]^{-2/3}. \quad \textbf{(14)}$$

Practically, the measurements $I(\theta)$ are linked to $p_{\mathrm{MHG}}(\theta)$ through a scaling factor K. Then, Eq. (14) could be rewritten as

$$[I(\theta) - K f p(\theta)]^{-2/3} = [1 + g_{\mathrm{HG}}^2 - 2g_{\mathrm{HG}}\cos\theta]\left[\frac{K(1-f)(1-g_{\mathrm{HG}}^2)}{4\pi}\right]^{-2/3}. \quad \textbf{(15)}$$

Since the ratio $Kf/4\pi$ can be identified with b, $f = 4\pi b/K$. The right-hand side of Eq. (15) could be rearranged as a linear form $A + B\cos\theta$, where $A = (1 + g_{\mathrm{HG}}^2)C$, $B = -2g_{\mathrm{HG}}C$, and $C = [\frac{K(1-f)(1-g_{\mathrm{HG}}^2)}{4\pi}]^{-2/3}$.

Let us now obtain an equation for g_{HG}. From the ratio A/B, we get

$$1 + g_{\mathrm{HG}}^2 + 2\frac{A}{B}g_{\mathrm{HG}} = 0, \quad \textbf{(16)}$$

where only

$$g_{\mathrm{HG}} = -\frac{A}{B} - \sqrt{\left(\frac{A}{B}\right)^2 - 1} \quad \textbf{(17)}$$

has been retained among the two roots.

Figures 4(a) and 4(b) show the graphs of $[I(\theta) - b]^{-2/3}$ versus $\cos\theta$, resulting from experimental irradiation of a skin sample (Golden Delicious) at 852 nm and a flesh sample (Royal Gala) at 763 nm, respectively. For the scattering angle θ ranging from 0° to 45°, linear regression of the data in Fig. 4(a) (skin sample) shows that $[I(\theta) - b]^{-2/3}$ is linearly related to $\cos\theta$ as predicted in Eq. (15). In contrast, the data related to Fig. 4(b) (flesh sample) reveal a partial linear fit with another departure from $\theta = 6 - 8°$. The two distinct trends shown in Figs. 4(a) and 4(b) have been well confirmed for all studied skin and flesh samples, independently of their origin and the working wavelength. As suggested above [see Fig. 2(a)], the artifact, related to the partial linear fit observed for the flesh sample, may be imputed to a scattering regime change that occurs for small detecting angles ranging from 0 to 6°. Despite that, the slope

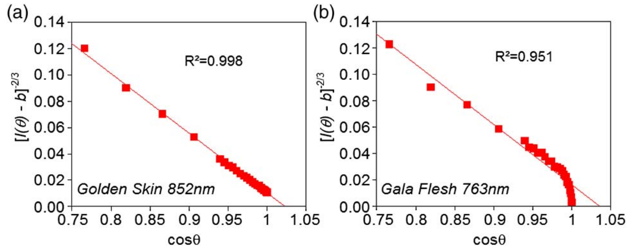

Fig. 4. Graphs of $[I(\theta) - b]^{-2/3}$ versus cos θ. (a) Skin sample extracted from a Golden Delicious, and irradiated at 852 nm. (b) Flesh sample extracted from a Royal Gala and irradiated at 763 nm. The straight lines in (a) and (b) are the least-squares fits for $[I(\theta) - b]^{-2/3}$ with regression coefficients R^2. The fitted data were obtained by extending the range of b up to $\theta = 55°$.

of the curves and their y-intercept yield reliable data for estimating A and B, and then g_{HG} by means of the Eq. (17). Next, using $C_{\exp} = -B/(2g_{\mathrm{HG}})$ and $f = 4\pi b/K$, we have

$$K = 4\pi b + \frac{4\pi C_{\exp}^{-3/2}}{1 - g_{\mathrm{HG}}^2} \tag{18}$$

and so the value of f.

Figures 5(a) and 5(b) depict the corresponding fits of the modified Henyey-Greenstein phase function, $p_{\mathrm{MHG}}(\theta)$, with the experimental data. It can be seen [Fig. 5(a)] that $p_{\mathrm{MHG}}(\theta)$ fits well the experiments (Skin/Golden Delicious/852 nm) from 0 to 85°, especially in the forward direction. However, there is a noticeable discrepancy between the data around $\theta = 90°$, and for $\theta > 150°$. For large scattering angles in the backward direction, the approximation $\sim\cos^2\theta$ seems not yet sufficient. In contrast, as shown in Fig. 5(b), the experiments (Flesh/Royal Gala/763 nm) are not well fitted around $\theta = 0°$, and for $60° \leq \theta \leq 110°$. These results have been obtained with (a) $g_{\mathrm{HG}} = 0.809 - f = 0.218$ and (b) $g_{\mathrm{HG}} = 0.766 - f = 0.292$.

From Fig. 6(a), it can be seen that the modified Henyey-Greenstein and Gegenbauer phase functions fit well the goniometric data of the Granny skin studied at $\lambda = 784$ nm, with relative errors of 5% ($g_{\mathrm{HG}} = 0.79 - f = 0.133$, $g_\alpha = 0.785 - f = 0.115 - \alpha = 0.614$). In return, the modified Henyey-Greenstein phase function [Fig. 6(b), dashed line] does not take into account the forward scattered light along the optical axis ($0 < \theta < 6°$), in the case of the flesh sample at the same wavelength ($g_{\mathrm{HG}} = 0.754 - f = 0.328$, $g_\alpha = 0.911 - f = 0.295 - \alpha = 10^{-5}$).

The use of the modified Mie phase function results in the best agreement between the calculated and experimental angular scattered intensities, for the flesh and skin of Granny studied at 633 nm [Figs. 7(a) and 7(b)] or at 763 nm [Figs. 7(c) and 7(d)]. For these fits, the following parameters were retrieved: (a) $g_{\mathrm{Mie}} = 0.656 - f = 0.57$, (b) $g_{\mathrm{Mie}} = 0.766 - f = 0.234$, (c) $g_{\mathrm{Mie}} = 0.658 - f = 0.238$, and (d) $g_{\mathrm{Mie}} = 0.723 - f = 0.168$.

The curves were generated using the six fitted parameters ρ_i listed in Table 2. For all studied cases, a complete set of fitted parameters (g_{HG}, f, g_α, α, and g_{Mie}) referring to the three modified scattering phase functions was established. These parameters are listed Tables 4–6 in Appendix C.

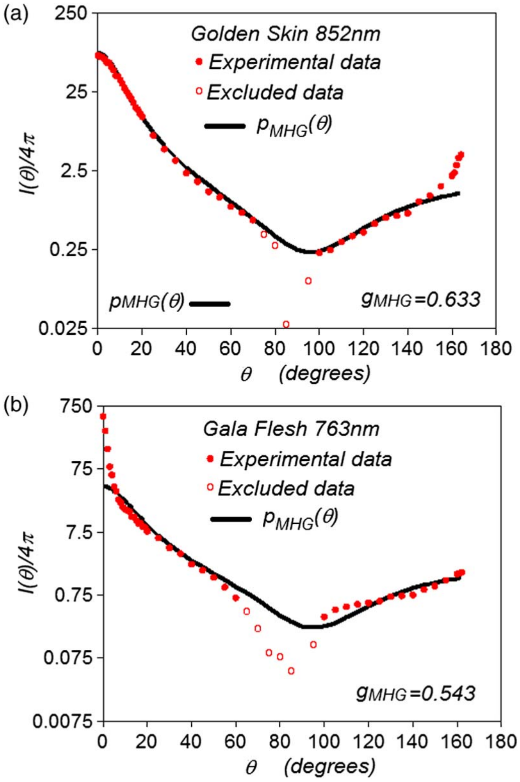

Fig. 5. Fits of the modified Henyey-Greenstein phase function $p_{\mathrm{MHG}}(\theta)$ on experimental goniometric data. (a) Skin sample (Golden Delicious) irradiated at 852 nm. (b) Flesh sample (Royal Gala) irradiated at 763 nm.

Figure 8 shows the distribution of g_{HG}, g_{GK}, g_{Mie}, and g_s as a function of the four working wavelengths 633, 763, 784, and 852 nm, for the flesh [(a), (c), and (e)] and the skin [(b), (d), and (f)] of the three apple cultivars. The fluctuation of

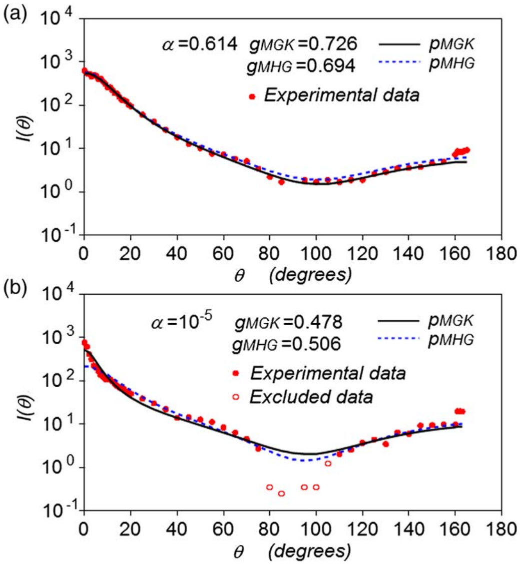

Fig. 6. Examples of goniometric data related to (a) skin and (b) flesh samples (Granny Smith/784 nm), fitted with the modified Henyey-Greenstein function (dashed line) and the Gegenbauer kernel phase function (full line).

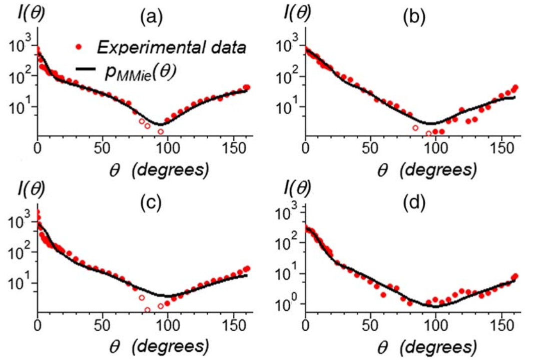

Fig. 7. Examples of goniometric data related to flesh, (a) Granny Smith/633 nm and (c) Granny Smith/763 nm, and skin, (b) Granny Smith/633 nm and (d) Granny Smith/763 nm, fitted with the modified Mie phase function.

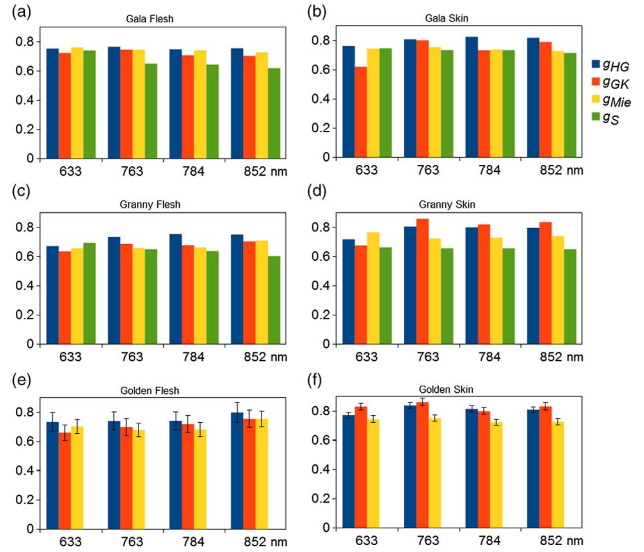

Fig. 8. Distribution of the anisotropy factors g_{HG}, g_{GK}, and g_{Mie} according to the wavelength for all the tissues studied. The coefficient g_S estimated from Ref. [14] is added (last column) for the cases of Granny Smith and Royal Gala.

the anisotropy factors, shown in Fig. 8, can be attributed to the studied tissue type and the working wavelength, but also to the measurement technique. It can be observed that the error bars are always larger for the flesh [see Fig. 8(e)] in comparison with those of the skin [Fig. 8(f)]. This may be largely due to a structural matrix difference between these two tissue types, with a low signal-to-noise ratio in cases of flesh experiment.

Notice also that g_{HG} and g_{GK} values obtained at 763, 784, and 852 nm are generally slightly larger than those obtained at 633 nm, whereas g_{Mie} appears less affected by the working wavelength. It may be restated that wavelengths around 763, 784, and 852 nm provide information mainly on the light scattering in apple tissues, while fruit tissues absorb most light sources in the region of the absorption band of chlorophyll (~670 nm) [5,6,8]—and then, to a certain degree, at the wavelength of 633 nm. Consequently, less scattered light at 633 nm has the effect to slightly decrease the retrieved g_{HG} and g_{GK} values in the forward direction [see especially the case of Granny Smith, Fig. 8(d)]. Since Mie theory is based on particle size parameter and refractive index (see Appendix B), it results from this that the scattering coefficient μ_s decreases more smoothly when increasing the wavelength. In consequence, the anisotropy factor distribution of g_{Mie} are a bit less fluctuating than those corresponding to g_{HG} and g_{GK} in the range of 633–852 nm. Moreover, the g_{Mie} values match well the g_S values reported in Ref. [14], especially for the skin tissue of Royal Gala and the flesh tissue of Granny Smith.

Table 2. Relative Particle Densities Related to the Mie Coefficients Used in Fig. 7

r_i (μm)	**0.15**	**0.3**	**0.6**	**0.9**	**1.2**	**1.5**
	ρ_1/ρ_6	ρ_2/ρ_6	ρ_3/ρ_6	ρ_4/ρ_6	ρ_5/ρ_6	ρ_6/ρ_6
Flesh 763 nm	4.4×10^3	3×10^{-7}	1.7	1.4×10^{-7}	0.86	1
Flesh 633 nm	4.3×10^3	4.6×10^{-5}	0.96	4.9×10^{-6}	0.95	1
Skin 763 nm	1.4×10^{-3}	60	14	43	39	1
Skin 633 nm	1.3×10^3	76	31	1.7×10^{-9}	3.5×10^{-7}	1

4. DISCUSSION

In this paper, experimental and fitting methods have been presented to determine the single scattering anisotropy of thin tissue samples (skin and flesh) extracted from three apple varieties. These methods use goniometer measurements and the fit of three modified scattering phase functions to compute the effective anisotropy coefficient g_{eff} and to estimate the single anisotropy coefficient of each studied sample. However, it is well known that tissue thickness affects the angular light distribution and the fitted scattering phase function when samples are greater than one scattering length, i.e., $1/\mu_s$ [23]. Because it is difficult to play on the thickness of the skin sample (while avoiding a remaining flesh layer), Monte Carlo simulations were performed considering five thicknesses of the skin ($t = 75$, 100, 127, 150, and 200 μm) and of the flesh ($t = 150$, 200, 286, 330, and 400 μm). The optical parameters of these samples were adapted from Ref. [14], $\mu_s = 13.33\ \mathrm{mm}^{-1}$ for the skin and $\mu_s = 3.5\ \mathrm{mm}^{-1}$ for the flesh, with $\mu_a = 0.01\ \mathrm{mm}^{-1}$, and the refractive index tissue $n_{\mathrm{tissue}} = 1.33$ (relative refractive index $n_r = 1$).

For each simulation, 10^6 photons were launched at one side of the studied sample. The data listed in Table 3 include the two reference thicknesses (75 μm, skin; 286 μm, flesh) for which the optical thickness $\mu_s t$ is equal to 1. The optical thickness was varied in the range [1–2.66] for the skin and in the range [0.52–1.4] for the flesh. In both cases, it is shown that the computed g_{eff} and g_{forw} decrease as the optical thickness is increased. However, the values of g_{forw} are less influenced by the thickness of the sample than the values of g_{eff}. This is also shown in Figs. 9(a) and 9(b), where scattering-angular light distributions have been generated with the Monte Carlo code for four thicknesses of the tissue sample (flesh and skin). Note that the scattering light part in the forward direction is less sensitive to the thickness of the sample than the backward part.

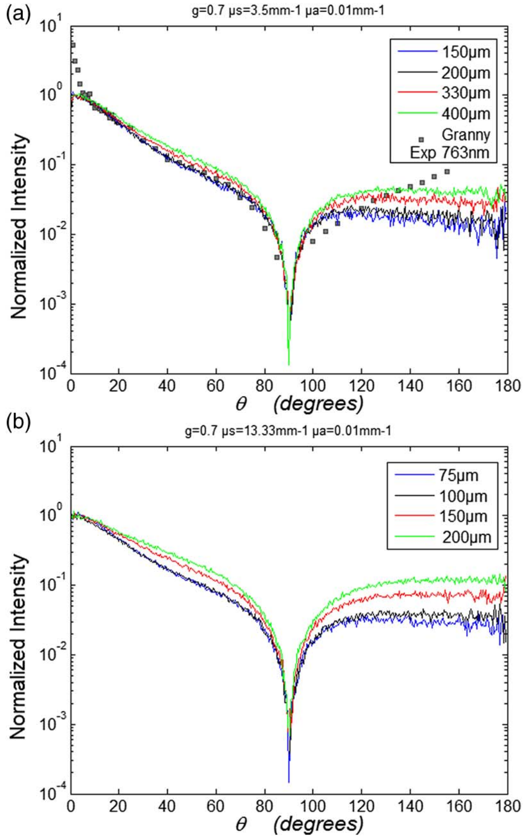

Fig. 9. Synthetic scattering-angular light distributions for four thicknesses of the tissue sample: (a) flesh (the square symbols refer to experiments performed with the Granny at 763 nm) and (b) skin.

The relative errors Δg_{eff} and Δg_{forw} for the flesh amount to (10%–26%) and (0–10%), respectively, when the optical thickness of the sample is varied from 0.52 to 1.4. For the skin, the relative errors Δg_{eff} and Δg_{forw} are greater and amount to (19%–48%) and (6%–23%), respectively, because the optical thickness range is more extended [1–2.66]. The refractive indices of these tissue samples are expected within 1.35–1.4 [14] at the considered wavelengths. Using $n_{\mathrm{tissue}} = 1.4$ ($n_r = 1.05$), the Monte Carlo simulations performed with $t = 330$ μm for the flesh, and $t = 75$ μm for the skin, still show the relative errors Δg_{eff} and Δg_{forw} equal to 24% and 5% for the flesh and 22% and 8% for the skin, respectively. We also note [Fig. 9(a)] that simulation and experimental results (Granny Smith, flesh, 763 nm) are close in the forward direction, but with a less agreement in the backward direction, when $g = 0.7$ is taken into account in the Monte Carlo code. This shows that the Henyey-Greenstein phase function is mainly suitable in the forward direction.

In all studied theoretical cases (Table 3), we note that the errors related to g_{forw} are less than those linked to g_{eff}. This suggests that g_{forw} is closer to the true single anisotropy than g_{eff} for an optical thickness around 1 when the scattering is far from the isotropic trend (i.e., $g > 0.6$). Because the phase functions p_{HG}, p_{GK}, and p_{Mie} (included in the modified phase functions) were intended to fit the forward part of the experimental data, their anisotropy factor g_{HG}, g_{GK}, and g_{Mie} should be close to the single anisotropy. Furthermore, the Mie phase function p_{Mie} is based on physical values (particle radii) corresponding to those of fruits. The scattering process inside the apple is well related to scattering particles interacting with the light: cell walls, air pores, and cellular content (vacuoles, starch granules, and chloroplasts [21]). The match, previously noted between the g_{Mie} values and the g_S reference values, confirms this fact.

On the whole, this work confirms the forward peaked nature of the scattering in both apple tissues, skin and flesh, with $g = 0.6 - 0.8$ (600–800 nm), in good agreement with the results reported by Saeys *et al.* [14], or with certain scattering optical properties of red onion [37]. However, it disagrees with a more recent study [38], which noticed a high overall anisotropy factor with values around 0.97 and 0.93 at 800 nm for the skin and flesh, respectively. A possible explanation may be due to an overestimation of the scattering coefficient μ_s measured by these authors.

Knowledge of the scattering phase function $p(\theta)$, and the anisotropy $g = \langle \cos\theta \rangle$, is important when spatially resolved reflectance measurements are used in optical inspection of highly diffusing materials. That is especially the case of the apples when the structure is investigated by means of a hand-held optics probe in spatially resolved mode, where the source–detector separation is ~1 mm [15]. With this probe configuration, small volumes of biological tissues can be explored, and then optically characterized. However, the development of relevant models is needed for modeling light propagation in tissue, not only near the surface (skin–flesh), but also in depth (flesh). Other techniques such as optical coherence tomography used to visualize the microstructure of an apple peel [36] and the laser speckle technique revealing the ripening stage of fruits [39] may also be improved from the consideration of the shape of the scattering phase functions [21,40].

Future studies will exploit systematic measurements of scattering coefficients and scattering-angular light distributions in fruit tissues, with the objective of developing innovative approaches for tissue imaging at multiple wavelengths.

Table 3. Effect of Sample Thickness *t* (μm) on the Generated g_{eff} and g_{forw} by Monte Carlo Simulations

Flesh Sample[a]					Skin Sample[b]				
t	g_{eff}	Δg_{eff}	g_{forw}	Δg_{forw}	t	g_{eff}	Δg_{eff}	g_{forw}	Δg_{forw}
150	0.633	10%	0.698	0%	75	0.570	19%	0.660	6%
200	0.608	13%	0.683	2%	100	0.523	25%	0.636	9%
286	0.571	18%	0.661	6%	127	0.485	31%	0.610	13%
330	0.552	21%	0.649	7%	150	0.444	37%	0.586	16%
400	0.521	26%	0.631	10%	200	0.364	48%	0.541	23%

[a] $g = 0.7 - \mu_s = 3.5\ \mathrm{mm}^{-1}$, $n_r = 1 - \mu_a = 0.01\ \mathrm{mm}^{-1}$.

[b] $g = 0.7 - \mu_s = 13.33\ \mathrm{mm}^{-1}$, $n_r = 1 - \mu_a = 0.01\ \mathrm{mm}^{-1}$.

APPENDIX A

Nomenclature:

g_{eff}	effective anisotropy coefficient
g_{forw}	forward anisotropy coefficient
p_{MHG}	modified Henyey-Greenstein phase function

p_{HG}	single Henyey-Greenstein phase function
g_{MHG}	anisotropy coefficient (modified Henyey-Greenstein phase function)
g_{HG}	anisotropy coefficient (single Henyey-Greenstein phase function)
p_{MGK}	phase function (modified Gegenbauer kernel phase function)
p_{GK}	phase function (single Gegenbauer kernel phase function)
g_{MGK}	anisotropy coefficient (modified Gegenbauer kernel phase function)
g_{GK}	anisotropy coefficient (single Gegenbauer kernel phase function)
g_{α}	parameter related to the single Gegenbauer kernel phase function
α	parameter related to the single Gegenbauer kernel phase function
f	weighting factor related to the term $(3/4\pi)\cos^2\theta$
$p_{M\mathrm{Mie}}$	phase function (modified scattering Mie phase function)
p_{Mie}	phase function (scattering Mie phase function)
$g_{M\mathrm{Mie}}$	anisotropy coefficient (modified scattering Mie phase function)
g_{Mie}	anisotropy coefficient (scattering Mie phase function)
P_i	Mie scattering function of a spherical particle i
x_i	size parameter size of a spherical particle i
$\mu_{s,i}$	scattering coefficient of a spherical particle i

APPENDIX B

$$P_{\mathrm{Mie}} = x_i^{-2}\left\{\left|\sum_{k=1}^{\infty}\frac{(2k+1)}{k(k+1)}\left[a_k\frac{P_k^1(\cos\theta)}{\sin\theta} + b_k\frac{dP_k^1(\cos\theta)}{d\theta}\right]\right|^2 + \left|\sum_{k=1}^{\infty}\frac{(2k+1)}{k(k+1)}\left[b_k\frac{P_k^1(\cos\theta)}{\sin\theta} + a_k\frac{dP_k^1(\cos\theta)}{d\theta}\right]\right|^2\right\}, \tag{B1}$$

$$a_k = \frac{m_1\psi(m_1x)\psi'(m_2x) - m_2\psi(m_2x)\psi'(m_1x)}{m_1\zeta(m_1x)\psi'(m_2x) - m_2\psi(m_2x)\zeta'(m_1x)};$$
$$b_k = \frac{m_2\psi(m_1x)\psi'(m_2x) - m_1\psi(m_2x)\psi'(m_1x)}{m_2\zeta(m_1x)\psi'(m_2x) - m_1\psi(m_2x)\zeta'(m_1x)}, \tag{B2}$$

where $x_i = 2\pi r_i/\lambda$, λ is the wavelength, r_i is the particle radius, m_1 is the extern refractive index, m_2 is the particle refractive index, P_k^1 is the associated Legendre polynomial, ψ and ζ are the Riccati–Bessel functions of first and second kind.

APPENDIX C

Table 4. Modified Henyey-Greenstein Phase Function: Fitted Relevant Parameters (g_{HG}, f)

	Gala Flesh		Golden Flesh		Granny Flesh		Gala Skin		Golden Skin		Granny Skin	
λ (nm)	g_{HG}	f	g_{HG}	f	g_{HG}	f	g_{HG}	f	g_{HG}	f	g_{HG}	f
633	0.753	0.325	0.734	0.418	0.671	0.475	0.763	0.266	0.771	0.215	0.718	0.180
763	0.766	0.291	0.740	0.377	0.734	0.311	0.809	0.274	0.838	0.269	0.805	0.174
784	0.749	0.242	0.741	0.297	0.754	0.328	0.827	0.22	0.814	0.195	0.800	0.133
852	0.755	0.170	0.799	0.374	0.751	0.351	0.819	0.292	0.809	0.218	0.797	0.149

Table 5. Modified Gegenbauer Phase Function: Fitted Relevant Parameters (g_{α}, α, f)

	Gala Flesh			Golden Flesh			Granny Flesh			Gala Skin			Golden Skin			Granny Skin		
λ (nm)	g_{α}	α	f	g_{α}	α	f	g_{α}	α	f	g_{α}	α	f	g_{α}	α	f	g_{α}	α	f
633	0.946	2.0E – 7	0.295	0.895	2.9E – 6	0.295	0.870	5.0E – 7	0.295	0.856	7.E – 6	0.205	0.742	0.806	0.265	0.820	0.157	0.265
763	0.961	5.3E – 6	0.265	0.928	5.0E – 7	0.295	0.917	4.0E – 7	0.295	0.820	0.451	0.295	0.789	0.754	0.295	0.788	0.747	0.205
784	0.934	4.7E – 6	0.205	0.943	2.0E – 7	0.295	0.911	1.1E – 5	0.295	0.859	0.192	0.175	0.818	0.444	0.235	0.785	0.614	0.115
852	0.931	1.2E – 6	0.085	0.966	5.5E – 6	0.295	0.932	5.7E – 6	0.295	0.847	0.345	0.265	0.793	0.622	0.265	0.766	0.739	0.115

Table 6. Modified Mie Phase Function: Fitted Relevant Parameters (g_{Mie}, f)

	Gala Flesh		Golden Flesh		Granny Flesh		Gala Skin		Golden Skin		Granny Skin	
λ (nm)	g_{Mie}	f	g_{Mie}	f	g_{Mie}	f	g_{Mie}	f	g_{Mie}	f	g_{Mie}	f
633	0.761	0.212	0.703	0.302	0.656	0.570	0.745	0.208	0.744	0.166	0.766	0.234
763	0.745	0.229	0.678	0.323	0.658	0.238	0.755	0.187	0.751	0.236	0.723	0.168
784	0.741	0.216	0.681	0.210	0.663	0.261	0.739	0.136	0.723	0.121	0.730	0.108
852	0.728	0.102	0.754	0.210	0.710	0.338	0.728	0.158	0.727	0.182	0.740	0.132

Funding. Region des Pays de la Loire AI-Fruit Project.

REFERENCES

1. V. V. Tuchin, I. L. Maksimova, D. A. Zimnyakov, I. L. Kon, A. H. Mavlyutov, and A. A. Mishin, "Light propagation in tissues with controlled optical properties," J. Biomed. Opt. **2**, 401–417 (1997).
2. V. V. Tuchin, *Tissue Optics: Light Scattering Methods and Instruments for Medical Diagnosis*, 2nd ed. (SPIE, 2007).
3. S. L. Jacques, "Optical properties of biological tissues: a review," Phys. Med. Biol. **58**, R37–R61 (2013).
4. B. Nicolaï, K. Beullens, E. Bobelyn, A. Peirs, W. Saeys, K. Theran, and J. Lammertyn, "Nondestructive measurement of fruit and vegetable quality by means of NIR spectroscopy: a review," Postharvest Biol. Technol. **46**, 99–118 (2007).
5. R. Cubeddu, C. D'Andrea, A. Pifferi, P. Taroni, A. Torricelli, G. Valentini, and C. Valero, "Nondestructive quantification of chemical and physical properties of fruits by time-resolved reflectance spectroscopy in the wavelength range 650–1000 nm," Appl. Opt. **40**, 538–543 (2001).
6. R. Cubeddu, C. D'Andrea, A. Pifferi, P. Taroni, A. Torricelli, G. Valentini, M. Ruiz-Altisent, C. Valero, C. Ortiz, C. Dover, and D. Johnson, "Time-resolved reflectance spectroscopy applied to the nondestructive monitoring of the internal optical properties in apples," Appl. Spectrosc. **55**, 1368–1374 (2001).
7. M. Vanoli, A. Rizzolo, P. E. Zerbini, L. Spinelli, A. Torricelli, G. Valentini, and D. Johnson, "Non-destructive detection of internal defects in apple fruit by time-resolved reflectance spectroscopy," in *Environmentally Friendly and Safe Technologies for Quality of Fruit and Vegetables* (2010), pp. 20–26.
8. J. Qin and R. Lu, "Measurement of the optical properties of fruits and vegetables using spatially resolved hyperspectral diffuse reflectance imaging technique," Postharvest Biol. Technol. **49**, 355–365 (2008).
9. H. Cen and R. Lu, "Quantification of the optical properties of two-layer turbid materials using a hyperspectral imaging-based spatially-resolved technique," Appl. Opt. **48**, 5612–5623 (2009).
10. M. L. Askoura, V. Piron, F. Vaudelle, J. P. L'Huillier, E. Madieta, and E. Mehinagic, "Experimental investigation on light propagation through apple tissue structures," Proc. SPIE **9542**, 954218 (2015).
11. X. Fu and Y. Ying, "Food safety evaluation based on near-infrared spectroscopy and imaging: a review," Crit. Rev. Food Sci. Nutr. **56**, 1913–1924 (2014).
12. M. Patterson, B. Chance, and B. C. Wilson, "Time-resolved reflectance and transmittance method for the non-invasive measurement of tissue optical properties," Appl. Opt. **28**, 2331–2336 (1989).
13. T. J. Farrell, M. S. Patterson, and B. Wilson, "A diffusion theory model of spatially resolved, steady-state diffuse reflectance for the noninvasive determination of tissue optical properties in vivo," Med. Phys. **19**, 879–888 (1992).
14. W. Saeys, M. A. Velazco-Roa, S. N. Thennadil, H. Ramon, and B. M. Nicolaï, "Optical properties of apple skin and flesh in the wavelength range from 350 to 2200 nm," Appl. Opt. **47**, 908–919 (2008).
15. N. Nguyen Do Trong, C. Erkinbaev, M. Tsuta, J. De Baerdemaeker, B. Nicolaï, and W. Saeys, "Spatially resolved diffuse reflectance in the visible and near-infrared wavelength range for non-destructive quality assessment of 'Braeburn' apples," Postharvest Biol. Technol. **91**, 39–48 (2014).
16. L. H. Wang, S. L. Jacques, and L. Q. Zheng, "MCML-Monte Carlo modeling of light transport in multilayered tissues," Comput. Methods Prog. Biol. **47**, 131–146 (1995).
17. D. A. Boas, J. Culver, J. Stott, and A. Dunn, "Three dimensional Monte Carlo code for photon migration through complex heterogeneous media including the adult human head," Opt. Express **10**, 159–170 (2002).
18. F. Vaudelle and J. P. L'Huillier, "Time-resolved optical fluorescence spectroscopy of heterogeneous turbid media with special emphasis on brain tissue structures including diseased regions: a sensitivity analysis," Opt. Commun. **304**, 161–168 (2013).
19. F. Vaudelle and J. P. L'Huillier, "Influence of the size and skin thickness of apple varieties on the retrieval of internal optical properties using Vis/NIR spectroscopy: a Monte Carlo-based study," Comput. Electron. Agric. **116**, 137–149 (2015).
20. M. L. Askoura, F. Vaudelle, and J. P. L'Huillier, "Numerical study of light transport in apple models based on Monte Carlo simulations," Photonics **3**, 2 (2016), doi: 10.3390/photonics3010002.
21. R. Watté, B. Aernouts, R. Van Beers, E. Herremans, Q. Tri Ho, P. Verboven, B. Nicolaï, and W. Saeys, "Modeling the propagation of light in realistic tissue structures with MMC-fpf: a meshed Monte Carlo method with free phase function," Opt. Express **23**, 17467–17486 (2015).
22. A. Fernandez-Oliveras, M. Rubino, and M. M. Perez, "Scattering anisotropy measurements in dental tissues and biomaterials," J. Eur. Opt. Soc. **7**, 12016 (2012).
23. S. L. Jacques, C. A. Alter, and S. A. Prahl, "Angular dependence of HeNe laser light scattering by human dermis," Laser Life Sci. **1**, 309–334 (1987).
24. D. Fried, R. E. Glena, J. D. B. Featherstone, and W. Seka, "Nature of light scattering in dental enamel and dentin at visible and near-infrared wavelengths," Appl. Opt. **34**, 1278–1285 (1995).
25. S. T. Flock, B. C. Wilson, and M. S. Patterson, "Total attenuation coefficients and scattering phase functions of tissues and phantom materials at 633 nm," Med. Phys. **14**, 835–841 (1987).
26. J. Choukeife and J. P. L'Huillier, "Measurements of scattering effects within tissue-like media at two wavelengths of 632.8 nm and 680 nm," Lasers Med. Sci. **14**, 286–296 (1999).
27. R. Marchesini, A. Bertoni, S. Andreola, E. Melloni, and A. E. Sichivollo, "Extinction and absorption coefficients and scattering phase functions of human tissues *in vitro*," Appl. Opt. **28**, 2318–2324 (1989).
28. P. Saccomandi, V. Vogel, B. Bazrafshan, J. Maurer, E. Schena, T. J. Vogl, S. Silvestri, and W. Mäntele, "Estimation of anisotropy coefficient of swine pancreas, liver and muscle at 1064 nm based on goniometric technique," J. Biophoton. **8**, 422–428 (2015).
29. L. I. Chaikovskaya, O. V. Tsarjuk, I. V. Belotserkovsy, and M. A. Vozmitel, "Determination of optical properties of tissues," J. Quant. Spectrosc. Radiat. Transfer **112**, 2128–2133 (2011).
30. G. Hall, S. L. Jacques, K. W. Eliceiri, and P. J. Campagnola, "Goniometric measurements of thick tissue using Monte Carlo simulations to obtain the single scattering anisotropy coefficient," Biomed. Opt. Express **3**, 2707–2719 (2012).
31. L. G. Henyey and J. L. Greenstein, "Diffuse radiation in the galaxy," Astrophys. J. **93**, 70–83 (1941).
32. G. W. Kattawar, "A three-parameter analytic phase function for multiple scattering calculations," J. Quant. Spectrosc. Radiat. Transfer **15**, 839–849 (1975).
33. F. Bevilacqua and C. Depeursinge, "Monte Carlo study of diffuse reflectance at source–detector separations close to one transport mean free path," J. Opt. Soc. Am. A **16**, 2935–2945 (1999).
34. L. O. Reynolds and N. J. McCormick, "Approximate two-parameter phase function for light scattering," J. Opt. Soc. Am. **70**, 1206–1212 (1980).
35. C. F. Bohren and D. R. Huffman, *Absorption and Scattering of Light by Small Particles* (Wiley, 1983).
36. P. Verboven, A. Nemeth, M. K. Abera, E. Bongaers, D. Daelemans, P. Estrade, E. Herremans, M. Hertog, W. Saeys, E. Vanstreels, B. Verlinden, M. Leitner, and B. Nicolaï, "Optical coherence tomography visualizes microstructure of apple peel," Postharvest Biol. Technol. **78**, 123–132 (2013).
37. W. Wang and C. Li, "Measurement of the light absorption and scattering properties of onion skin and flesh at 633 nm," Postharvest Biol. Technol. **86**, 494–501 (2013).
38. R. Van Beers, B. Aernouts, R. Watté, A. Schenk, B. Nicolai, and W. Saeys, "Evolution of Vis/NIR bulk optical properties of apple skin and flesh during fruit maturation," in *Proceedings of the 17th International Conference on Near Infrared Spectroscopy* (2015).
39. R. Nassif, F. Pellen, C. Magne, B. Le Jeune, G. Le Brun, and M. Abboud, "Scattering through fruits during ripening: laser speckle technique correlated to biochemical and fluorescence measurements," Opt. Express **20**, 23887–23897 (2012).
40. S. Malektaji, I. T. Lima, Jr., and S. S. Sherif, "Monte Carlo simulation of optical coherence tomography for turbid media with arbitrary spatial distributions," J. Biomed. Opt. **19**, 046001 (2014).